Earth Planet. Sci. Lett. 658 (2025) 119288

Contents lists available at ScienceDirect

Earth and Planetary Science Letters

journal homepage: www.elsevier.com/locate/epsl

On the emergence of fault afterslip during laboratory seismic cycles

Corentin Noël [a,*], Cédric Twardzik [a], Pierre Dublanchet [b], François Passelègue [a]

[a] Université Côte d'Azur, CNRS, Observatoire de la Côte d'Azur, IRD, Géoazur, Valbonne, France
[b] Mines Paris, PSL University, Center for Geosciences and Geoengineering, Fontainebleau, France

ARTICLE INFO

Editor: J.P. Avouac

Dataset link: https://zenodo.org/records/13912519

Keywords:
Fault heterogeneity
Seismic cycle
Post-seismic deformation
Afterslip

ABSTRACT

Spatial fault heterogeneity is often invoked to explain the occurrence of fault afterslip following seismic ruptures. In this study, we tested this hypothesis in the laboratory by performing triaxial experiments on both homogeneous and heterogeneous faults, under confining pressures of 30, 60, and 90 MPa. The faults were composed of granite, prone to seismic behaviour, and marble, prone to aseismic behaviour. Unlike homogeneous granite faults, which display a nucleation stage followed by regular seismic events, heterogeneous faults can contain the co-seismic dynamic event within the experimental fault length. During this phase, the aseismic areas adjacent to the dynamic event undergo a stress increase, which is then released by fault afterslip over an extended post-seismic phase. The magnitude and duration of this post-seismic phase increase with confining pressure and with the proportion of aseismic-prone areas. We infer that the enhancement of post-seismic afterslip originates from the increase in the frictional stability of the aseismic-prone area, and of the normal stress acting on the fault. In addition, the observed increase in initial strain rate with normal stress is well explained by the rate-and-state framework. At the scale of our experiments, fault frictional heterogeneities play a primary role in the emergence of fault afterslip.

1. Introduction

Recent geodetical and seismological observations have revealed that a significant proportion of earthquakes exhibit prolonged fault afterslip, primarily characterized by aseismic fault movement in the surrounding of the seismically ruptured zone (e.g., Barbot et al., 2009; Cheloni et al., 2010; Smith and Wyss, 1968; Yagi et al., 2001, 2003. See Avouac (2015) for an extensive review). Importantly, the moment released by fault afterslip can be as large as, or even larger than the co-seismic moment (Barbot et al., 2009). Because of that, fault afterslip is expected to contribute significantly to the energy release along the fault during the seismic cycle, as well as to stress transfer in areas devoid of recent seismic rupture.

To understand the physical parameters controlling the emergence of fault afterslip, numerical models have been developed, primarily based on rate-and-state friction laws (Dieterich, 1978; Ruina, 1983). Within this framework, fault afterslip is typically explained by spatial frictional heterogeneities, where velocity-weakening and velocity-strengthening regions interact (Marone et al., 1991; Rice and Gu, 1983). In these models, the co-seismic event is confined to the velocity-weakening zone, which induces stress perturbations and a slip deficit in the velocity-strengthening region, that is subsequently retrieved (at least partially) by aseismic fault afterslip, and often associated with aftershocks (Perfettini and Avouac, 2007). Other models suggest that the presence of stress heterogeneities can induce the emergence of fault afterslip (Helmstetter and Shaw, 2009; Hirose and Hirahara, 2004). In this case, afterslip can occur on a velocity-weakening fault zone presenting a stress level that is too low to trigger earthquakes or to permit the adjacent rupture to propagate through this area. Finally, a recent study suggests that fault afterslip can be generated on any portion of the fault presenting a geometric moment deficit (the product of slip and rupture area) following an earthquake (Meade, 2024). While these models can effectively describe fault afterslip following earthquakes (e.g., Barbot et al., 2009; Fukuda et al., 2009; Gualandi et al., 2017; Helmstetter and Shaw, 2009; Lin et al., 2013; Perfettini et al., 2010; Perfettini and Avouac, 2004, 2007; Wimpenny et al., 2017), assumptions are needed in order to estimate the physical parameters that govern fault afterslip, especially due to the unknown stress conditions.

To understand further the emergence of fault afterslip, laboratory experiments have been conducted along homogeneous and heterogeneous fault interfaces. For example, Caniven et al. (2015) demonstrated that post-seismic deformation (both afterslip and viscoelastic relaxation)

* Corresponding author.
E-mail address: corentin.noel@geoazur.unice.fr (C. Noël).

https://doi.org/10.1016/j.epsl.2025.119288
Received 10 October 2024; Received in revised form 11 February 2025; Accepted 21 February 2025
0012-821X/© 2025 The Authors. Published by Elsevier B.V. This is an open access article under the CC BY license (http://creativecommons.org/licenses/by/4.0/).

can be observed in a strike-slip heterogeneous fault system only, composed of a polyurethane foam placed on a silicone layer, representing the seismic upper crust and the ductile lower crust, respectively. Similarly, in analogue experiment of subduction systems, introducing viscoelastic coupling between the overriding plate and the mantle wedge facilitates the post-seismic viscoelastic relaxation phase (Caniven and Dominguez, 2021). On bare rock interfaces, afterslip has been observed due to pore fluid pressure recharge of the fault following a co-seismic event (Aben and Brantut, 2023). In this scenario, afterslip is co-located with the main rupture zone, contrary to what is typically observed in natural earthquakes. Afterslip has also been observed, though to a limited extent, on large bi-axial faults composed of homogeneous granite interface (Ke et al., 2021). When ruptures are confined, limited afterslip occurs at the rupture arrest tip, releasing about 5% of the stress deficit, which is significantly smaller than what is observed for large earthquakes (Barbot et al., 2009; Cheloni et al., 2010; Smith and Wyss, 1968; Yagi et al., 2001, 2003). To our knowledge, laboratory experiments conducted on bare rock interfaces have not yet reproduced large afterslip similar to what is observed after large natural earthquakes, which is characterized by significant slip amplitude occurring outside of co-seismic slip patch.

Here, we tackle this issue by conducting laboratory triaxial experiments of homogeneous and heterogeneous faults composed of Westerly granite (prone to seismic behaviour) and Carrara marble (prone to aseismic behaviour) (Figure S1). The experiments were performed at confining pressure (P_c) ranging from 30 to 90 MPa to investigate the effect of different depth on heterogeneous fault's seismic cycle. These experiments allowed, for the first time, to reproduce afterslip in a triaxial apparatus, and to estimate the parameters controlling the distribution of fault slip during the different stages of the seismic cycle.

2. Experimental methods

Two lithologies were used for the study: Westerly granite (Rhode Island, USA) and Carrara marble (Tuscany, Italy). These lithologies were selected because they are well studied in the literature (Fredrich et al., 1989; Lockner, 1998; Schmid et al., 1980; Tullis and Yund, 1977; Wong, 1982) and have opposite frictional properties. Under the tested conditions, laboratory experiments show that bare surface fault of Westerly granite are prone to seismic behaviour (Lockner et al., 2017; Passelègue et al., 2016; Thompson et al., 2009), related to a velocity weakening behaviour (Dieterich, 1979; Ruina, 1983). On the contrary, in the tested conditions, Carrara marble is prone to aseismic behaviour (Aubry et al., 2020; Carpenter et al., 2016; Verberne et al., 2014), related to velocity-strengthening behaviour, and can experience a brittle-ductile transition at high confining pressure ($P_c > 50$ MPa (Fredrich et al., 1989; Meyer et al., 2019)).

The tested samples are cylinders of 39.5-mm diameter and 85-mm height, with a saw-cut oriented at 30° from the cylinder axis. Five samples, composed of homogeneous and heterogeneous half-sample, were tested: (i) granite-on-granite fault (G_f), (ii) granite-on-granite with a marble inclusion (M_{inc}), (iii) granite-on-marble with a granitic inclusion (G_{inc}), (iv) granite-on-marble fault (GM_f), and (v) marble-on-marble fault (M_f) (Figure S1). The inclusion are 12-mm diameter cores inserted into the cylindrical samples. The faults surfaces (i.e., saw-cut surfaces) were then polished using a silicon carbide powder with grains having a 5-μm diameter (equivalent to #1200 grit).

All experiments were conducted in a triaxial loading apparatus located in Géoazur and developed by CoreLabs (Brantut et al., 2011; Passelègue et al., 2016). Both axial and radial pressure were monitored using pressure transducers (±50-kPa resolution). The axial displacement (d_{ax}) was measured using three external gap sensors, placed outside of the confining cell, having a 0.1-μm resolution. The axial displacement was corrected from the apparatus and sample stiffness (ranging from 290 to 560 MPa/mm depending on the sample and P_c conditions), and projected to the fault surface to obtain the fault displacement (d_{fault}). In addition, 8 strain gauges were deployed around the fault (Figure S2), allowing to record local strain measurement during the sample deformation. These strain gauges were glued parallel to the axial stress (σ_{ax}) as close as possible to the fault (typically their centre stands at 5 mm from the fault plane). Note that the strain gauges were always glued on the granite half sample (except for the M_f), to insure measurement on a homogeneous medium. During the sample deformation, all the mechanical data were recorded at 2400 Hz sampling rate. An experiment consists in two main steps. After placing the fault assemblage into the deformation apparatus, we first conducted successive deformation at 30, 60 and 90 MPa confining pressure. For each of the tested confining pressure conditions, the deformation of the sample was conducted by applying a constant flux of 100 cc/hr at the axial pump, corresponding to an almost constant far field axial velocity of 1.4×10^{-3} mm/s. During these three consecutive stages, the roughness of the fault is expected to evolve with the cumulative displacement and with the increase of stress at fault asperities. Because of that, in a second step, we conducted two additional experiments, decreasing first the confining pressure back to 60 MPa, and finally to 30 MPa. In the following, we mainly focus on the experiments conducted during the stepwise increase of confining pressure. The results of the experiments in which the confining pressure was decreased stepwise will be discussed in the Section 4 only. For additional information on the experimental methods, please refer to the Supplementary Material section 1.

3. Experimental results

3.1. Macroscopic measurements

The experimental results show that the fault slip behaviour depends primarily on the sample composition (Fig. 1), and secondarily on the confining pressure. As expected, our two end-members tested fault show opposite behaviour. G_f shows typical repeated stick-slip (i.e., seismic) behaviour with macroscopic shear stress drop ($\Delta\tau$) increasing from ~ 3.3 to 14.8 MPa with increasing P_c from 30 to 90 MPa. In these experiments, most of the slip occurs seismically (Fig. 2a), as observed in previous studies (Lockner et al., 2017; Passelègue et al., 2016; Thompson et al., 2009). Conversely, M_f shows stable sliding behaviour for all the tested P_c. The heterogeneous samples (G_{inc}, M_{inc}, and GM_f) all show repeated stick-slip behaviour. Interestingly, the macroscopic stress drop is decreasing with increasing marble content (Fig. 1 and Table S1–3). For example, at $P_c = 30$ MPa, $\Delta\tau$ is reduced from ~ 1.5 MPa for M_{inc} to 1 MPa for G_{inc}. For all the heterogeneous samples, increasing the confining pressure favour larger macroscopic stress drop (Fig. 1 and Table S1–3).

To analyse further the influence of heterogeneities on the different stages of the seismic cycle, we now describe the evolution of the shear stress and of the fault slip before, during and after the main instabilities. For all the experiments, the inter-seismic phase is characterized by an elastic stage, highlighted by a linear increase in shear stress during which no slip is observed (Fig. 2). This phase ends when the shear stress reaches a critical value allowing the initiation of fault slip. At this point, the faults enter in a pre-seismic phase (or nucleation phase), which is characterized by a deviation from linearity in the macroscopic shear stress, and by the onset of fault slip (yellow areas, Fig. 2a-d). The amount of slip during the pre-seismic phase remains small, but is systematically observed. The duration of the nucleation phase and the measured slip are larger for G_f when compared to the other tested fault. Increasing the confining pressure tends to increase both the duration and the amount of slip accumulated during the pre-seismic phase (Fig. 2e-g). Following the nucleation phase, a rapid macroscopic stress drop associated with rapid fault slip is observed (Fig. 2a-d). This fast fault slip phase, corresponding to a far-field slip rate typically greater than 1 mm/s, is defined as co-seismic. As expected from the values of the stress drop, increasing the content of marble leads to a decrease of the co-seismic slip (Fig. 2). For G_f, the amount of co-seismic slip increases from 34 to 116 μm with increasing the confining pressure from 30 to 90 MPa (Fig. 2e-g). For the

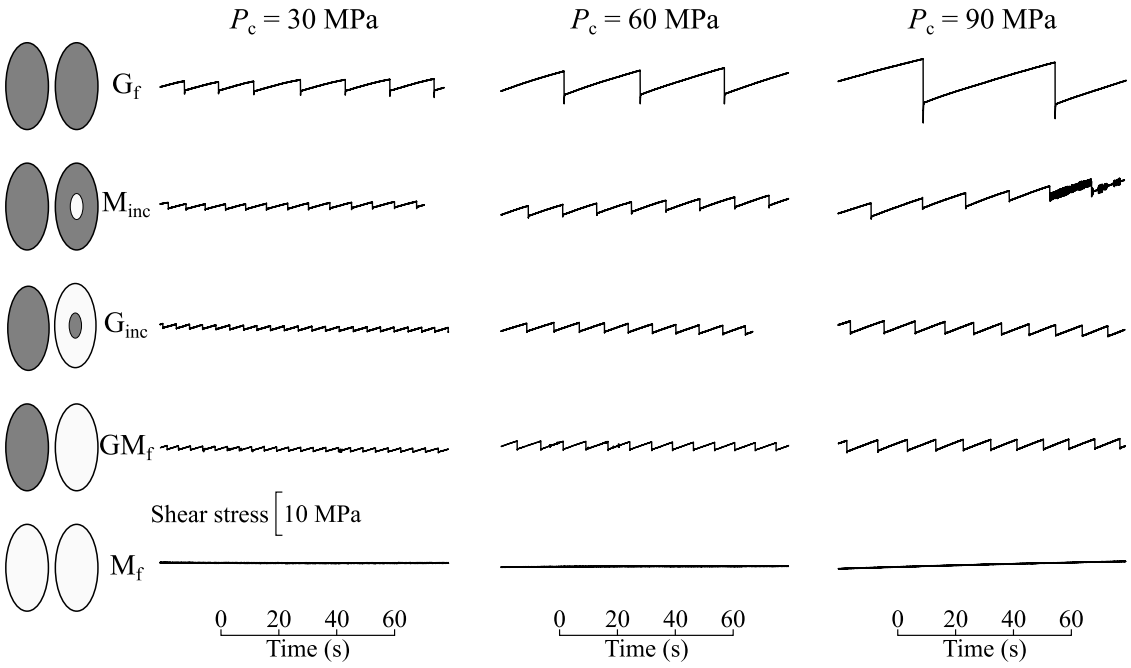

Fig. 1. Shear stress measured as a function of time for the 5 tested fault compositions and three tested confining pressures. The symbols of the left represent the two sides of the fault tested (grey for granite and white for marble). Note that the shear stress and time axes are the same for all the data plotted. For the full mechanical curves see Figure S4 in the supplementary material. Also note that, for the heterogeneous sample, the macroscopic shear stress drop measurements are an average of the entire fault. Because of that, the real co-seismic stress drop must be larger than the apparent measurement presented here when the seismic rupture is confined within the fault.

heterogeneous fault (M_{inc}, G_{inc} and GM_f), the amount of co-seismic slip is about 7–15 μm in average at P_c = 30 MPa, and of 13–25 μm at higher confining pressure (Fig. 2e-g).

The main result of our study is that following the co-seismic phase, heterogeneous faults exhibit an extended period of slip (Fig. 2). This behaviour is particularly well observed for G_{inc} and GM_f, where fault slip continues after the co-seismic phase over a non-negligible amount of time (from 1 to 1.5 second at P_c = 90 MPa, blue areas in Fig. 2c and d). Remarkably, in the case of G_f, no fault afterslip is observed. Our results demonstrate that the presence of a single marble inclusion (M_{inc}) allows fault afterslip to take up to 10% of the total slip (i.e., pre-, co- and post-seismic slip, Fig. 2e-g). Increasing the content of marble tends to enhance fault afterslip. G_{inc} and GM_f show the largest and the longest afterslip stages. For these faults, afterslip represent up to 28% of the total slip. Additionally, the fault afterslip increases with P_c, increasing for example from 17% to 27% with increasing P_c from 30 to 90 MPa for G_{inc} (Fig. 2e-g).

3.2. Local strain measurements

To analyse the slip distribution during the different stages of the seismic cycle, the array of strain gauges measuring axial strain variation close to the fault was used. In the following the influence of heterogeneity on the nucleation, co-seismic and post-seismic phases are described using this array.

3.2.1. Nucleation of instability

As observed in the macroscopic measurements (Fig. 2), the initiation of the nucleation stage is highlighted by the strain gauges array when the inelastic strain (see Supplementary Material section 1.4) departs from 0 indicated by a horizontal broken line on Fig. 3 and Fig. 4. Note that a decrease in inelastic strain is a proxy for fault slip, while an increase in inelastic strain is a proxy for fault stick (or slipping less than the rest of the fault). The nucleation stage is clearly marked for G_f, where the onset of nucleation, associated with the propagation of a quasi-static slip front, can be tracked spatially. The quasi-static slip front initiates in the upper part of the fault (blue curves on Fig. 3a-c, blue and green curves on Fig. 4a and Figure S7a-c) and propagates toward the bottom of the fault (Fig. 3a-c and Fig. 4a).

In the case of heterogeneous fault, the nucleation stage is more complicated. For M_{inc}, at confining pressures of 30 and 60 MPa, the initiation of the pre-seismic phase is more localized at the granite-granite contacts (Figure S7d-f). Meanwhile, inelastic strain near the marble inclusion (yellow and green curves in Figure S7d-f) is increasing, indicating that this part of the fault remains locked. However, at P_c = 90 MPa, the nucleation is predominantly confined to the bottom left of the sample (orange curve in Fig. 4b), while other parts of the fault remain locked. For G_{inc}, the pre-seismic phase is primarily confined to the bottom of the granite inclusion (orange curve in Fig. 3g-i, Fig. 4c and Figure S7g-i), while the rest of the fault experiences an increase in strain. Note that for this sample, an aborted pre-seismic phase could also be observed on the top of the inclusion (green curve on Fig. 4c). Finally, for GM_f, the pre-seismic phase is mainly confined to the bottom of the fault, with the top part remaining locked (Fig. 3j-l, Fig. 4d and Figure S7j-l). Notably, for all tested fault and confining pressure conditions, the onset of the nucleation phase coincides with the location of maximum recorded stress (Figures S10 and S11), i.e., where the static friction is the highest.

3.2.2. Co-seismic phase

The strain gauges array can be used to track the propagation of the seismic rupture (Passelègue et al., 2020). For G_f, the dynamic strain drop occurs at the same time on all the strain gauges (Fig. 3a-c, Fig. 4a and Figure S7a-c). Our temporal resolution does not allow us to see any propagation of this strain drop front, which means that the front must propagate at least at 190 m/s, and that the co-seismic rupture propagates through the entire fault.

For M_{inc}, the dynamic strain drop also occurs on all the strain gauges at the same time, indicating fast rupture velocity. Additionally, at P_c = 90 MPa, the two strain gauges located at the top of the sample measure

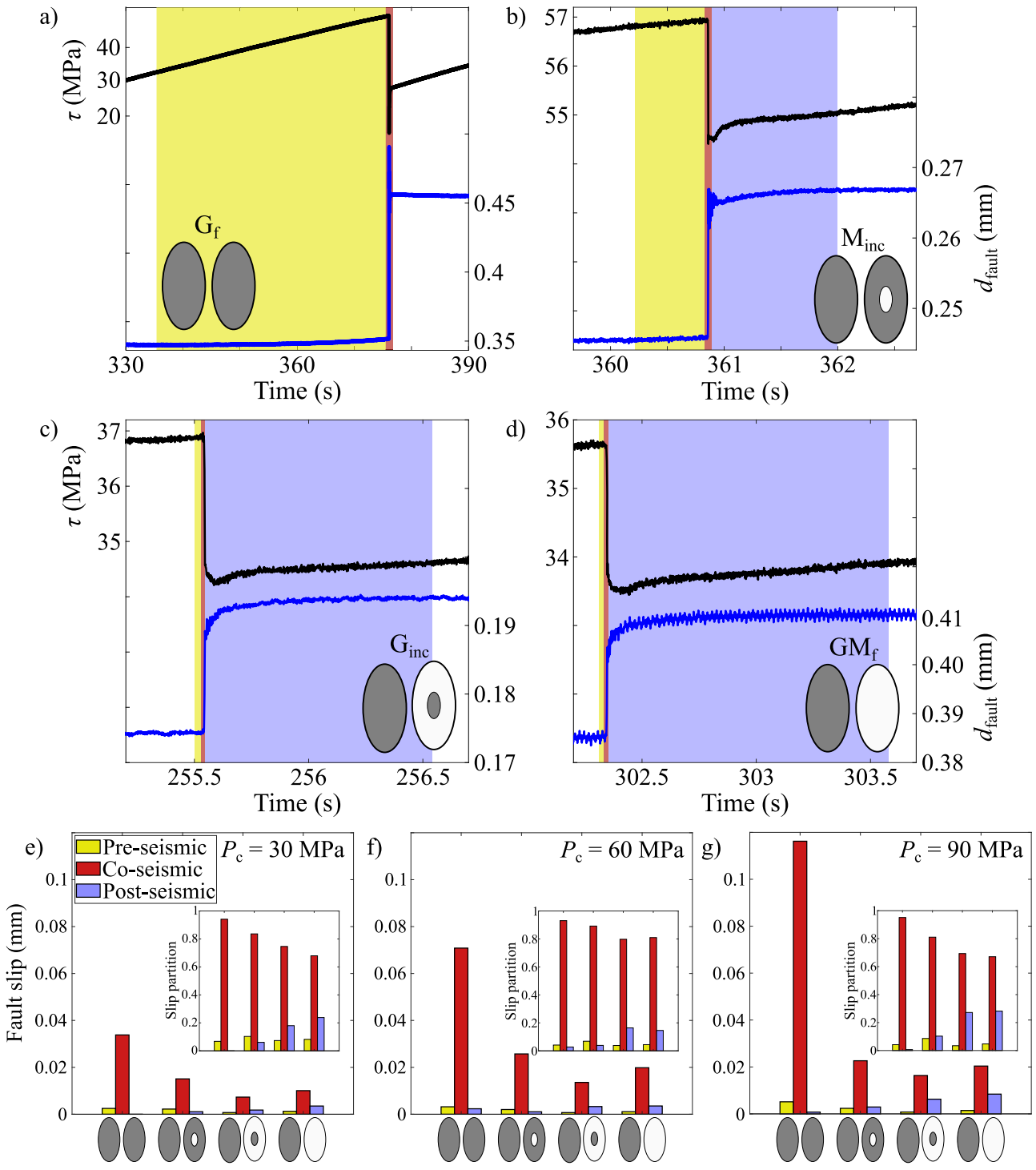

Fig. 2. a-d) Shear stress (black curves) and fault displacement (blue curves) as a function of time measured during a typical event at P_c = 90 MPa on a) granite-on-granite (G_f), b) granite-on-granite with marble inclusion (M_{inc}), c) granite-on-marble with granite inclusion (G_{inc}), and d) granite-on-marble (GM_f) samples. The yellow, red and blue zones represent the pre-seismic, co-seismic and post-seismic phases, respectively. e-g) Fault slip (average of all the events) recorded during pre-seismic, co-seismic and post-seismic phases for the tested fault that experienced seismic behaviour for e) P_c = 30 MPa, f) P_c = 60 MPa and g) P_c = 90 MPa. The symbols of the x-axis represent the two sides of the fault tested (grey for granite and white for marble). In each plot, the insert represents the fault slip distribution for each tested condition.

an increase in strain rather than a drop (Fig. 4b) suggesting that this part of the fault did not break co-seismically. In the case of G_{inc}, a rapid strain drop is observed only on the strain gauges located close to the granite inclusion (i.e., at the centre of the fault, Fig. 4c). Strain gauges located further from the inclusion experience a large increase in strain. Finally, for GM_f, the co-seismic strain drop is also confined close to the nucleation zone (orange curves on Fig. 3j-l and Fig. 4d). For G_{inc} and GM_f, increasing the confining pressure favour a smaller spatial extent of the co-seismic rupture (Figure S7j-l). For G_{inc}, at P_c = 30 and 60 MPa fast strain drop ($> 2 \times 10^{-2}$ /s) extends from the top left to the bottom right of the fault surface (green, yellow and orange curves on Figure S7 g and h) while at P_c = 90 MPa, fast strain drop is only measurable at two strain

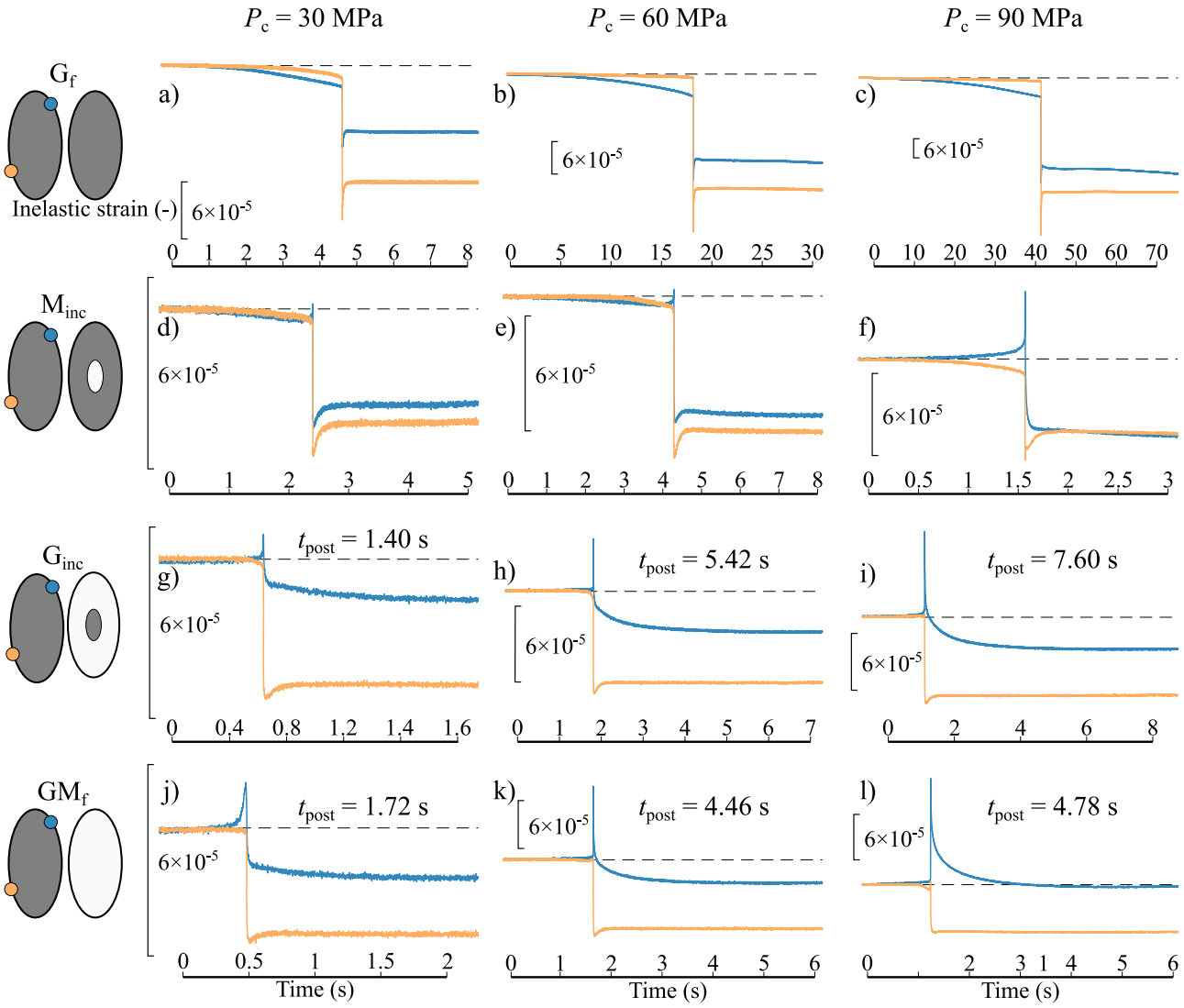

Fig. 3. Inelastic strain measurement obtained from two strain gauges as a function of time for the tested fault composition. SG5 (orange), having often the larger co-seismic strain drop; and SG2 (blue) having often the largest post-seismic long-term strain drop. For each case, a typical seismic event is presented. The symbols of the left represent the two sides of the fault tested (grey for granite and white for marble). a-c) G_f, d-f) M_{inc}, g-i) G_{inc}, j-l) GM_f. a, d, g, j) P_c = 30 MPa, b, e, h, k) P_c = 60 MPa and c, f, i, l) P_c = 90 MPa. Note that the inelastic strain scale is different for each plot. The colour of the curve represents the strain gauge position on the sample schematic. See Fig. 4 and Figure S7 in the supplementary material for the data measured at all the strain gauges. For G_{inc} and GM_f (g-l), the duration of the post-seismic phase (t_{post}) is indicated. It represents the time from the end of the co-seismic strain drop to the moment at which all the inelastic strain as a function of time returns flat.

gauges located at the bottom of the fault surface close to the granite inclusion (orange curves on Fig. 4c and Figure S7i). For GM_f, at Pc = 30 and 60 MPa, fast strain drops extend on the left and top right part of the fault surface (green, yellow and orange curves on Figure S7j and k), whereas they are more restricted to the bottom left of the fault surface (orange and yellow curve on Fig. 4d and Figure S7l).

3.2.3. *Afterslip phase*

The strain gauges array also recorded the signal of fault afterslip during the post-seismic stage. For the heterogeneous samples (particularly for the ones with high marble content), after the co-seismic phase, some strain gauges show a long strain release (Fig. 3, Fig. 4 and Figure S7). This long strain release is located in areas devoid of co-seismic strain drop, i.e., where a strain deficit has accumulated during the co-seismic phase.

For G_{inc}, the strain gauges located far from the seismic granite inclusion exhibit a large increase of strain during the co-seismic phase (Fig. 3g-I and Fig. 4c). During the post-seismic phase, these same strain gages (blue curves in Fig. 3g-i, blue and red curves in Fig. 4c), are subjected to a long-lasting strain decay. The same behaviour is observed for GM_f for the strain gages located far from the co-seismic strain drop (Fig. 3j-l and Fig. 4d). As observed on the macroscopic data, the post-seismic phase is particularly well developed at high P_c. Increasing P_c from 30 to 90 MPa, the duration of the post-seismic phase increases from ~1 to ~7 s and from ~1 to ~4 s for G_{inc} and GM_f, respectively. Similarly, post-seismic phase seems to emerge for M_{inc} at large confining pressure (blue curve in Fig. 3f). This result demonstrates that the post-seismic phase, associated with afterslip is mostly observed far from the co-seismic strain drop areas (Figure S8), and well captured by local strain gauges measurements (Fig. 3g-l, Fig. 4c and d).

In summary, the macroscopic and strain gauge data show that the spatial and temporal evolution of slip and strain is more complex for heterogeneous faults than for homogeneous ones. In particular, the nucleation phase of heterogeneous faults is reduced in time and space compared to G_f (deviation from the broken line on Fig. 3 and Fig. 4). However, heterogeneities favour local stress/strain changes

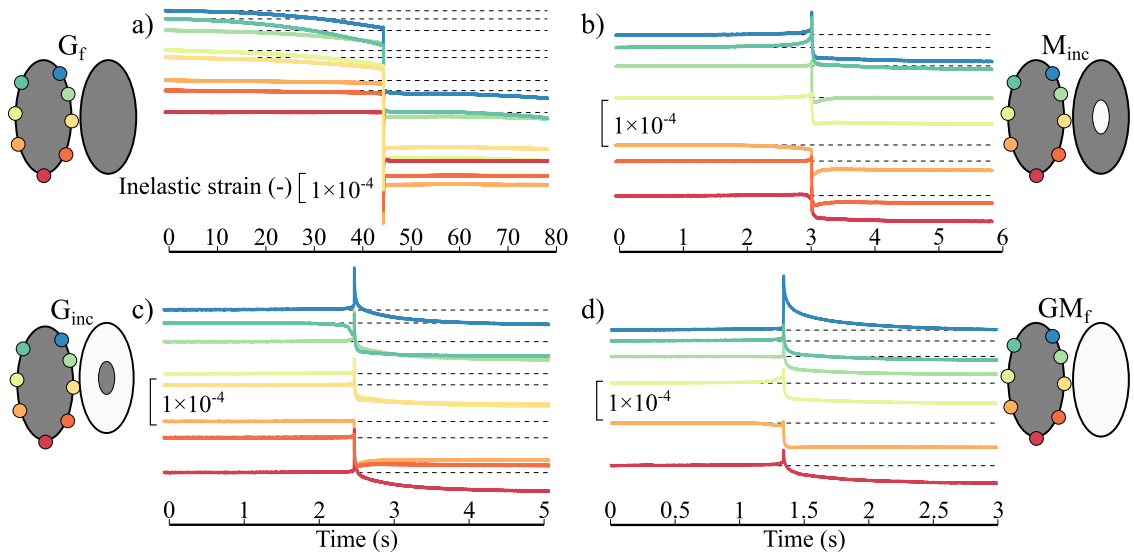

Fig. 4. Inelastic strain measurement obtained from the eight strain gauges as a function of time for the tested fault composition at 90 MPa of confining pressure. For each case, a typical seismic event is presented. The symbols of the left represent the two sides of the fault tested (grey for granite and white for marble). a) G_f, b) M_{inc}, c) G_{inc}, d) GM_f. Note that the inelastic strain scale is different for each plot. The colour of the curve represents the strain gauge position on the sample schematic. See Figure S7 in the supplementary material for the data at all tested confining pressure.

subsequently to the co-seismic phase (i.e., confined stress/strain drop), that give rise to a stress/strain deficit at the edge of the rupture (blue curves on Fig. 3). This stress/strain deficit favour the emergence of fault afterslip (blue curves on Fig. 3).

4. Discussion

Our experiments highlight that frictional heterogeneities are able to modify the seismic cycle of a simple geometry fault. Particularly, granite-granite contacts favour the release of the accumulated stress through dynamic events. Instead, for the granite-marble contact, stress is released not only through dynamic events, but also through fault afterslip during a post-seismic phase. This behaviour is observed at all the tested confining pressures. However, higher confining pressures tend to favour fault afterslip of larger magnitude that last longer (Fig. 2, Fig. 3 and S9). Our experiments are in this sense in agreement with rate-and-state models proposed for afterslip (Marone et al., 1991), as frictional heterogeneities are needed (or at least help) for the emergence of afterslip.

As stated previously, we find that fault afterslip is preferentially observed on strain gauges that exhibits little to no dynamic co-seismic strain drop (Figure S8). These results agree with observations from natural earthquake, where afterslip tends to occur in region devoid of co-seismic slip (Barbot et al., 2009; Gualandi et al., 2017; Hsu et al., 2002; Lu and Zhou, 2022; Miyazaki et al., 2004; Perfettini and Avouac, 2007) or with a little overlap (Barnhart et al., 2016; Hsu et al., 2006, 2009; Lin et al., 2013; Ozawa et al., 2012; Twardzik et al., 2021; Wimpenny et al., 2017).

Our experiments suggest that for afterslip to take place during our experiments, two mutually dependent conditions are required: (i) a seismic event confined within the experimental fault length, and (ii) a zone around the co-seismic rupture that is critically loaded and prone to aseismic behaviour, i.e., velocity strengthening. In our case, these conditions are favoured along the granite-marble contacts. Particularly, the case of G_{inc} sample demonstrates that frictional heterogeneities can be a key parameter for large afterslip (Fig. 2, Fig. 3g-l and Fig. 4c).

However, the bi-material fault experiment (GM_f) is more puzzling. Even if the fault is composed of two materials, the frictional property of this bi-material interface should be homogeneous across the fault, and should therefore produce only seismic or only aseismic slip. However, the behaviour is similar to G_{inc}, i.e., dynamic events are confined within the fault length, and fault afterslip occurs in areas devoid of co-seismic rupture (Fig. 3j-l). A possible explanation could be that stress heterogeneity (Figure S10 and S11 in the supplementary material) induce highly localized spatial frictional changes of the interface, and a transition from velocity strengthening to velocity weakening behaviour along the fault due to plastic processes at the scale of asperities, as observed previously in calcite-rich bare surface (Aubry et al., 2020). The second hypothesis is the development of a patch of granite rich fault gouge along the interface, allowing a dynamic instability to nucleate and propagate locally (Figure S12 in the supplementary material).

To understand further the dynamics of fault afterslip, we analyse our post-seismic data within the rate-and-state framework. For that, we used the strain gauge measurements, in which the transition between co-seismic and post-seismic phase is clearly identified as it is separated in space and time (Fig. 3 and Fig. 4). To prevent possible contamination of afterslip motion by the co-seismic rupture, we assume that the fault afterslip begins at the end of the rapid strain drop recorded by the strain gauge located the closest to the dynamic rupture (Figure S14). We consider the end of the post-seismic phase when the inelastic strain rate at the strain gauges goes back visually to 0. In this rate-and-state framework, we assume that all the strain released during the post-seismic phase occurs on the frictional interface, and that nothing is released within the bulk of the sample, which is commonly assumed for natural events. Note that for the performed experiments, this assumption seems reasonable as no bulk deformations has been observed on the post-mortem analysis of M_f and G_{inc} samples. We model the slipping region as a spring-slider system obeying rate-and-state friction (Dieterich, 1979; Ruina, 1983). Assuming steady-state approximation and that the loading rate during this phase is negligible, the strain relaxation during post-seismic deformation on a frictional interface can be described as (Helmstetter and Shaw, 2009; Marone et al., 1991; Scholz, 2019):

$$\varepsilon = \dot{\varepsilon}_0 t_0 \ln\left(\frac{t}{t_0}+1\right), \tag{1}$$

With

$$t_0 = \frac{\sigma_n (a-b)^*}{(k/K)\dot{\varepsilon}_0} \tag{2}$$

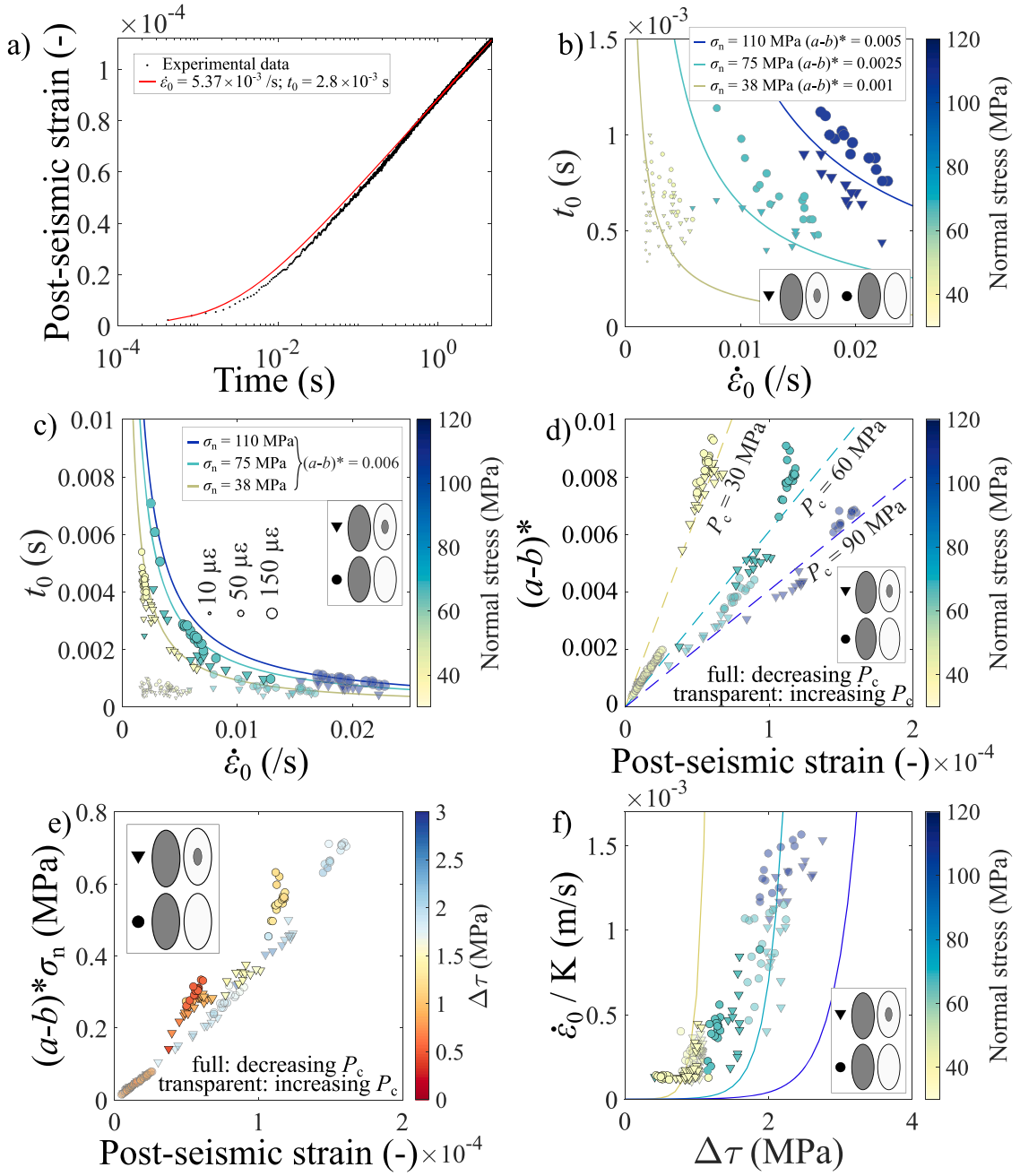

Fig. 5. a) Post-seismic strain as a function of time measured experimentally at one strain gauge SG2, along with the modelled one using Eq. (1). Here, the experimental data are for the strain measured at strain gauge 2 of the GM_f at $P_c = 60$ MPa. The red curve is the best fit using the experimentally retrieved $\dot{\varepsilon}_0$ and inverted t_0. The blue curve is the best fit inverting both $\dot{\varepsilon}_0$ and t_0. b) Measured strain rate at the onset of post-seismic phase $\dot{\varepsilon}_0$ as a function of the inverted t_0 for all the afterslip recorded at strain gauge for the experiments conducted during the stepwise increase of P_c. The solid lines correspond to the estimate of t_0 as a function of $\dot{\varepsilon}_0$ for the three average values of σ_n and $(a\text{-}b)^*$. c) Measured strain rate at the onset of post-seismic phase $\dot{\varepsilon}_0$ as a function of the inverted t_0 for all the afterslip recorded at strain gauge for the experiments conducted during the stepwise decrease of P_c. The data presented in figure b) are displayed in transparency. For panel b) and c), the size of the datapoint represent the total amplitude of post-seismic strain. d) Apparent rate-and-state parameter $(a\text{-}b)^*$ obtained from the inverted t_0 and the measured $\dot{\varepsilon}_0$, k and σ_n (Eq. (2)) as a function of the post-seismic strain. e) Same as panel d) except that $(a\text{-}b)^*$ is multiplied by the normal stress, allowing to collapse the data. The colour bar represents the macroscopic shear stress drop, $\Delta\tau$. f) Measured strain rate at the onset of post-seismic phase, as a function of the macroscopic shear stress drop, $\Delta\tau$. The full curves show $\frac{\dot{\varepsilon}_0}{K} = V_{pl}\exp\left[\frac{\Delta\tau}{(a-b)\sigma_n}\right]$, with V_{pl} being the far field loading rate (1.4 μm/s), $(a\text{-}b) = 0.003$, and for the three tested normal stress. For panels b-f) triangles and circles represent G_{inc} and GM_f, respectively. For panel c-f), the datapoint in transparency are the one obtained during the rising confining pressure step and the full datapoint are during the decreasing confining pressure step.

where σ_n is the normal stress acting on the fault, $(a\text{-}b)^*$ is the apparent steady-state rate-and-state parameter, k is the spring stiffness, K is a coefficient relating the change in axial strain with fault slip ($\varepsilon = K\delta$, δ being the slip), $\dot{\varepsilon}_0$ is the strain rate observed at the strain gauge location at the onset of afterslip, and t_0 is a characteristic time. The spring stiffness, k, relates the change in shear stress on the fault during the initial linear elastic loading of the sample, and is directly measured experimentally. The parameters K is estimated through finite elements analysis

following the method developed by Dublanchet et al. (2024). This approach accounts for the geometry of the fault and of the sample (See supplementary material section 7 for details). K depends on the strain gauge location, e.g., $K = 14.5\ m^{-1}$ for SG2.

In the model, we also fixed the initial strain rate $\dot{\varepsilon}_0$ to the value measured at the onset of fault afterslip on the strain gauge used. Therefore, we only invert for t_0. Eq. (1) provides a good fit of our experimental data (Fig. 5a and Figure S13), highlighting that the released strain related to fault afterslip evolves as a logarithmic function of time, as observed after natural earthquakes (e.g., Barbot et al., 2009; Cheloni et al., 2010; Smith and Wyss, 1968; Yagi et al., 2001). Note that using Eq. (1) and (2), only positive values of $(a\text{-}b)^*$ are considered, i.e., velocity strengthening behaviour. Other approximations exist involving negative values of $(a\text{-}b)^*$, i.e., velocity weakening behaviour, (Helmstetter and Shaw, 2009), however they imply stiffness or stress conditions that are not realistic for our performed experiments (for instance, $k > k_c$, where k_c is a critical stiffness; or $\tau \ll \tau_{ss}$, where τ_{ss} is the shear stress at steady state; see Helmstetter and Shaw, 2009 Table 2).

Assuming this hypothesis, the inversions conducted imposing our measurement of $\dot{\varepsilon}_0$ demonstrate at first order that, an increase in $\dot{\varepsilon}_0$ leads to a decrease in t_0 (Fig. 5b and 5c). Considering only the experiments conducted during the stepwise increase of P_c, we find that t_0 is slightly increasing with increasing confining pressure, for both G_{inc} and GM_f (Fig. 5b). In addition, t_0 is found to be generally larger for GM_f than for G_{inc}, in agreement with the increase in final strain released by fault afterslip. For both samples, the inverted t_0 are of the order of few milliseconds, that is, ~3 orders of magnitude shorter than the total duration of post-seismic phase. Assuming simply Eq. (2), this increase in t_0 is expected to result from an increase in $(a\text{-}b)^*$ with increasing confining pressure, since the increase in normal stress acting on the fault at each confining pressure tested is not enough to explain the observed trend (Fig. 5b). Interestingly, the trend is different for the experiments conducted during the stepwise decrease of P_c, i.e., decreasing the confining pressure from 90 MPa to 30 MPa (Fig. 5c). Once the fault surface has experienced stick-slip events and fault afterslip at $P_c = 90$ MPa, the frictional properties of the fault seem to remain constant, even when the confining pressure is decreased. For these experiments, the general trend in t_0 can be explained by Eq. (2), assuming simply the change in normal stress at the different confining pressure tested, and a similar value of $(a\text{-}b)^* = 0.006$ (Fig. 5c). Thus, during the stepwise increase of confining pressure, the general t_0-$\dot{\varepsilon}_0$ trend is influenced by both $(a\text{-}b)^*$ and P_c, whereas during the stepwise decrease of confining pressure, $(a\text{-}b)^*$ does not change and only P_c influences the relaxation time.

Interestingly, using the inverted values of t_0 and our direct experimental and numerical measurement of σ_n, k, K and $\dot{\varepsilon}_0$; we can use Eq. (2) to estimate $(a\text{-}b)^*$ for each event. Note that these estimates are expected to represent the frictional parameters during the afterslip phase, and representative of the granite-marble interface only, since we conducted the inversions only for G_{inc} and GM_f. We find that, an increase of post-seismic strain is observed with increasing $(a\text{-}b)^*$ (Fig. 5d). In addition, our results demonstrate that increasing the confining pressure (i.e., the normal stress) leads to an increase in $(a\text{-}b)^*$ for both G_{inc} and GM_f (transparency datapoint in Fig. 5d). This increase in $(a\text{-}b)^*$ could be directly related to an increase in $(a\text{-}b)$ (here rate-and-state parameters) of the marble-granite contact with increasing confining pressure. Indeed, the increase of $(a\text{-}b)^*$ with confining pressure is similar in magnitude than the increase in $(a\text{-}b)$ obtained for calcite gouge under the same normal stress conditions previously documented (Carpenter et al., 2016; Verberne et al., 2015). In agreement with the inverted values of t_0, GM_f presents generally larger values of $(a\text{-}b)^*$ and final post-seismic strain release (Fig. 5d). However, the events recorded at 60 MPa and 30 MPa confining pressure during the stepwise decrease of P_c (i.e., after the experiments conducted at 90 MPa confining pressure), exhibit larger post-seismic strain, and larger values in $(a\text{-}b)^*$ than the events conducted at the same confining pressure during the stepwise increase of P_c (Fig. 5d). Therefore, after a fault interface has undergone stick-slip events and afterslip at $P_c = 90$ MPa, its frictional properties retain a memory of the past deformation. Similar memory effect observations have been previously made on gouge samples (Hong and Marone, 2005; Pozzi et al., 2022; Scuderi et al., 2017), suggesting that our inversions of the apparent rate-and-state parameters, through our measurements of post-seismic strain release, are a real proxy for the frictional parameters of the fault at the strain gauge location. The increase of post-seismic strain with increasing $(a\text{-}b)^*$, or equivalently $(a\text{-}b)$, has been also demonstrated numerically. Specifically, if the $(a\text{-}b)$ parameter of a velocity strengthening region adjacent to a co-seismic stress perturbation is increased, the post-seismic slip increases proportionally to the total slip (Marone et al., 1991).

Remarkably, analysing all experiments together, the retrieved $(a\text{-}b)^*$ is directly proportional to the post-seismic strain for each tested confining pressure (Fig. 5d). At large confining pressure, similar values of post-seismic strain release require smaller $(a\text{-}b)^*$ values than at low confining pressure. These results trend to demonstrate that the amplitude of the strain release due to fault afterslip is mostly controlled by $\sigma_n(a\text{-}b)^*$. Indeed, multiplying each value of $(a\text{-}b)^*$ by the normal stress σ_n applied on the fault at the onset of post-seismic phase, collapses all the data set (Fig. 5e). Our results confirm that fitting the fault afterslip of real earthquakes can provide a good estimate of the local frictional parameters of the fault. However, since the normal stress (or effective normal stress) remains poorly constrained along natural faults, only the inversion of $\sigma_n(a\text{-}b)^*$ (as performed in some natural afterslip inversion studies, e.g., Lin et al., 2013; Perfettini et al., 2010; Perfettini and Avouac, 2004, 2007; Wimpenny et al., 2017) can provide an element of comparison between the different stations, or between different earthquakes.

Finally, our results also demonstrate that $\dot{\varepsilon}_0$ trend to increase with confining pressure (Fig. 5b and c), and with the average stress drop during instabilities (Fig. 5f). This increase in $\dot{\varepsilon}_0$ leads to the decrease in t_0 observed at each confining pressure, as expected by the theoretical predictions obtained from Eq. (2) (Fig. 5b and c). This increase in $\dot{\varepsilon}_0$ with P_c can be attributed to an increase in sliding velocity during the confined co-seismic ruptures. Indeed, the strain rate depends on the slip velocity time the parameter K ($\dot{\varepsilon} = KV_s$). As K is constant in the tested range of normal stress, $\dot{\varepsilon}$ is a direct function of the slip velocity reached at the onset of the fault afterslip. Following previous studies, the slip velocity at the onset of fault afterslip is expected to be a function of the stress drop and of the normal stress following $V_0 = V_{pl}\exp\left[\frac{\Delta\tau}{(a-b)\sigma_n}\right]$ (Perfettini and Ampuero, 2008; Perfettini and Avouac, 2007). Even if our measurement $\Delta\tau$ are obtained far from the fault (estimated from our pressure transducers), and therefore, potentially underestimated, our experimental results seem to confirm this exponential relationship between V_0 and $\Delta\tau$ (Fig. 5f). However, the role of $\dot{\varepsilon}_0$ on the final value of strain release during the post-seismic slip remains secondary compared to $\sigma_n(a\text{-}b)^*$ that has a predominant effect (Fig. 5e).

In summary, the evolution of the fault afterslip is well explained by the rate-and-state framework, and appears to be a combination of 1) the strain rate at the onset of afterslip $\dot{\varepsilon}_0$, which trend to decrease t_0 and 2) the frictional properties (i.e., $(a\text{-}b)^*$) around the area experiencing a dynamic stress/strain drop, which tends to increase with confining pressure.

For natural earthquakes, afterslip has been often proposed as the main driving force of the aftershock sequences (Avouac, 2015; Helmstetter and Shaw, 2009; and references therein). If the performed experiments do not allow to correlate afterslip and aftershock sequence (as no acoustic emission were emitted during afterslip sequences), they are able to identify the main parameters influencing the amplitude of afterslip. Our data alongside with recent experimental data performed on heterogeneous fault material (e.g., Arts et al., 2024; Bedford et al.,

2022; Song and McLaskey, 2024) highlight the major role of frictional heterogeneity on the fault strength and stability. In particular, they allow for the emergence of afterslip similar to the one occurring after large earthquakes.

5. Conclusion

Among the many hypotheses proposed for the generation of afterslip during natural events, this manuscript explores the role of frictional heterogeneities regarding the emergence of fault afterslip following large earthquakes. At the scale of our experiments, the presence of stress heterogeneities along the fault, which can potentially arrest seismic ruptures, does not appear sufficient to trigger a significant post-seismic phase. Instead, the emergence of afterslip in our experiments results from the interaction between a propagating seismic front, which stops in an aseismic region, causing a substantial increase in stress that is then released by fault afterslip. Our results are consistent with natural observations, including (i) afterslip occurring preferentially outside of the co-seismic rupture area, and (ii) a slip evolving with the logarithm of time. The measured afterslip in our experiments are explained by a simple model involving velocity-weakening patches, governed by a rate-and-state friction law, surrounded by a velocity-strengthening interface. This is supported by (i) the imposed rheology of our experimental faults, and (ii) the observed exponential increase in initial afterslip velocity with increasing stress drop. Finally, our results indicate that the afterslip magnitude is likely controlled by both the frictional properties of velocity-strengthening patches and the normal stress acting along the fault plane. Due to this complexity, independently analysing these parameters from natural afterslip measurements is expected to remain challenging, especially given the uncertain on the stress conditions along natural faults.

CRediT authorship contribution statement

Corentin Noël: Writing – original draft, Visualization, Methodology, Investigation, Formal analysis, Data curation, Conceptualization. **Cédric Twardzik:** Writing – review & editing, Visualization, Supervision, Formal analysis. **Pierre Dublanchet:** Writing – review & editing, Supervision, Formal analysis. **François Passelègue:** Writing – review & editing, Visualization, Validation, Supervision, Resources, Methodology, Investigation, Funding acquisition, Formal analysis, Conceptualization.

Declaration of competing interest

The authors declare that they have no known competing financial interests or personal relationships that could have appeared to influence the work reported in this paper.

Acknowledgment

This research has been founding by European Research Council (ERC) Starting Grant 101041966 (HOPE). The authors thanks Marie Violay for providing the sample and the sample preparation tools. The authors thanks Julien Ambre for the technical help in the laboratory. The authors thank Jean-Paul Ampuero, Allan Rubin, Federica Paglialunga and Barnaby Fryer for the fruitful discussion. FXP expresses his heartfelt gratitude to Alexandre Schubnel and Jérôme Fortin for generously donating the Sanchez triaxial press to him. The authors thank the editor Jean-Philippe Avouac, Georg Dresen and Vito Rubino for their constructive comments that have helped at improving the manuscript. Raw data can be found at https://zenodo.org/records/13912519.

Supplementary materials

Supplementary material associated with this article can be found, in the online version, at doi:10.1016/j.epsl.2025.119288.

Data availability

https://zenodo.org/records/13912519 (Raw data can be found at .)

References

Aben, F.M., Brantut, N., 2023. Rupture and afterslip controlled by spontaneous local fluid flow in crustal Rock. J. Geophys. Res.: Solid Earth 128 (11), e2023JB027534. https://doi.org/10.1029/2023JB027534.

Arts, J.P.B., Niemeijer, R., Drury, M.R., Willingshofer, E., Matenco, L.C., 2024. The frictional strength and stability of spatially heterogeneous fault gouges. Earth Planet. Sci. Lett. 628 (118586). https://doi.org/10.1016/j.epsl.2024.118586.

Aubry, J., Passelègue, F.X., Escartín, J., Gasc, J., Deldicque, D., Schubnel, A., 2020. Fault stability across the seismogenic zone. J. Geophys. Res.: Solid Earth 125 (8), e2020JB019670. https://doi.org/10.1029/2020JB019670.

Avouac, J.P., 2015. From geodetic imaging of seismic and aseismic fault slip to dynamic modeling of the seismic cycle. Annu Rev. Earth. Planet. Sci. 43, 233–271. https://doi.org/10.1146/annurev-earth-060614-105302.

Barbot, S., Fialko, Y., Bock, Y., 2009. Postseismic deformation due to the Mw 6.0 2004 Parkfield earthquake: stress-driven creep on a fault with spatially variable rate-and-state friction parameters. J. Geophys. Res.: Solid Earth 114 (B7). https://doi.org/10.1029/2008JB005748.

Barnhart, W.D., Murray, J.R., Briggs, R.W., Gomez, F., Miles, C.P.J., Svarc, J., Riquelme, S., Stressler, B.J., 2016. Coseismic slip and early afterslip of the 2015 Illapel, Chile, earthquake: implications for frictional heterogeneity and coastal uplift. J. Geophys. Res.: Solid Earth 121 (8), 6172–6191. https://doi.org/10.1002/2016JB013124.

Bedford, J.D., Faulkner, D.R., Lapusta, N., 2022. Fault rock heterogeneity can produce fault weakness and reduce fault stability. Nat. Commun. (326), 13. https://doi.org/10.1038/s41467-022-27998-2.

Brantut, N., Schubnel, A., Guéguen, Y., 2011. Damage and rupture dynamics at the brittle-ductile transition: the case of gypsum. J. Geophys. Res.: Solid Earth 116 (B1). https://doi.org/10.1029/2010JB007675.

Caniven, Y., Dominguez, S., 2021. Validation of a multilayered analog model integrating crust-mantle visco-elastic coupling to investigate subduction megathrust earthquake cycle. J. Geophys. Res.: Solid Earth 126 (2), e2020JB020342. https://doi.org/10.1029/2020JB020342.

Caniven, Y., Dominguez, S., Soliva, R., Cattin, R., Peyret, M., Marchandon, M., Romano, C., Strak, V., 2015. A new multilayered visco-elasto-plastic experimental model to study strike-slip fault seismic cycle. Tectonics 34 (2), 232–264. https://doi.org/10.1002/2014TC003701.

Carpenter, B.M., Collettini, C., Viti, C., Cavallo, A., 2016. The influence of normal stress and sliding velocity on the frictional behaviour of calcite at room temperature: insights from laboratory experiments and microstructural observations. Geophys. J. Int. 205 (1), 548–561. https://doi.org/10.1093/gji/ggw038.

Cheloni, D., D'Agostino, N., D'Anastasio, E., Avallone, A., Mantenuto, S., Giuliani, R., Mattone, M., Calcaterra, S., Gambino, P., Dominici, D., Radicioni, F., Fastellini, G., 2010. Coseismic and initial post-seismic slip of the 2009 Mw 6.3 L'Aquila earthquake, Italy, from GPS measurements. Geophys. J. Int. 181 (3), 1539–1546. https://doi.org/10.1111/j.1365-246X.2010.04584.x.

Dieterich, J.H., 1978. Time-dependent friction and the mechanics of stick-slip. Pure Appl. Geophys. 116 (4–5), 790–806. https://doi.org/10.1007/BF00876539.

Dieterich, J.H., 1979. Modeling of rock friction 1. Experimental results and constitutive equations. J. Geophys. Res.: Solid Earth 84 (B5), 2161–2168. https://doi.org/10.1029/JB084iB05p02161.

Dublanchet, P., Passelègue, F.X., Chauris, H., Gesret, A., Twardzik, C., Nöel, C., 2024. Kinematic inversion of aseismic fault slip during the nucleation of laboratory earthquakes. J. Geophis. Res.: Solid Earth 129 (12), e2024JB028733. https://doi.org/10.1029/2024JB028733.

Fredrich, J.T., Evans, B., Wong, T., 1989. Brittle to plastic transition in Carrara Marble. J. Geophis. Res. 94 (B4), 4129–4145. https://doi.org/10.1029/JB094iB04p04129.

Fukuda, J., Johnson, K.M., Larson, K.M., Miyazaki, S., 2009. Fault friction parameters inferred from the early stages of afterslip following the 2003 Tokachi-oki earthquake. J. Geophys. Res.: Solid Earth 114 (4). https://doi.org/10.1029/2008JB006166.

Gualandi, A., Avouac, J.P., Galetzka, J., Genrich, J.F., Blewitt, G., Adhikari, L.B., Koirala, B.P., Gupta, R., Upreti, B.N., Pratt-Sitaula, B., Liu-Zeng, J., 2017. Pre- and post-seismic deformation related to the 2015, Mw7.8 Gorkha earthquake, Nepal. Tectonophysics 714–715, 90–106. https://doi.org/10.1016/j.tecto.2016.06.014.

Helmstetter, A., Shaw, B.E., 2009. Afterslip and aftershocks in the rate-and-state friction law. J. Geophys. Res.: Solid Earth 114 (1). https://doi.org/10.1029/2007JB005077.

Hirose, H., Hirahara, K., 2004. A 3-D quasi-static model for a variety of slip behaviors on a subduction fault. Pure Appl. Geophys. 161, 2417–2431. https://doi.org/10.1007/s00024-004-2573-7.

Hong, T., Marone, C., 2005. Effects of normal stress perturbations on the frictional properties of simulated faults. Geochem., Geophys., Geosyst. 6 (3). https://doi.org/10.1029/2004GC000821.

Hsu, Y.-J., Bechor, N., Segall, P., Yu, S.B., Kuo, L.C., Ma, K.F., 2002. Rapid afterslip following the 1999 Chi-Chi, Taiwan earthquake. Geophys. Res. Lett. 29 (16), 1–4. https://doi.org/10.1029/2002GL014967.

Hsu, Y.-J., Simons, M., Avouac, J.-P., Galetzka, J., Sieh, K., Chlieh, M., Natawidjaja, D., Prawirodirdjo, L., Bock, Y., 2006. Frictional afterslip following the 2005 Nias-Simeulue earthquake, Sumatra. Science 312 (5782), 1921–1926. https://doi.org/10.1126/science.1126960.

Hsu, Y.-J., Yu, S.B., Chen, H.Y., 2009. Coseismic and postseismic deformation associated with the 2003 Chengkung, Taiwan, earthquake. Geophys. J. Int. 176 (2), 420–430. https://doi.org/10.1111/j.1365-246X.2008.04009.x.

Ke, C.Y., McLaskey, G.C., Kammer, D.S., 2021. The earthquake arrest zone. Geophys. J. Int. 224 (1), 581–589. https://doi.org/10.1093/gji/ggaa386.

Lin, Y.N.N., Sladen, A., Ortega-Culaciati, F., Simons, M., Avouac, J.P., Fielding, E.J., Brooks, B.A., Bevis, M., Genrich, J., Rietbrock, A., Vigny, C., Smalley, R., Socquet, A., 2013. Coseismic and postseismic slip associated with the 2010 Maule Earthquake, Chile: characterizing the Arauco Peninsula barrier effect. J. Geophys. Res.: Solid Earth 118 (6), 3142–3159. https://doi.org/10.1002/jgrb.50207.

Lockner, D.A., 1998. A generalized law for brittle deformation of Westerly granite. J. Geophys. Res.: Solid Earth 103 (B3), 5107–5123. https://doi.org/10.1029/97JB03211.

Lockner, D.A., Kilgore, B.D., Beeler, N.M., Moore, D.E., 2017. The transition from frictional sliding to shear melting in laboratory stick-slip experiments. Fault Zone Dynamic processes: Evolution of Fault Properties During Seismic Rupture, pp. 105–131.

Lu, L., Zhou, Y., 2022. Co- and post-seismic slip analysis of the 2017 MW7.3 Sarpol Zahab earthquake using Sentinel-1 data. Geod. Geodyn. 13 (2), 151–159. https://doi.org/10.1016/j.geog.2021.10.004.

Marone, C.J., Scholz, C.H., Bilham, R., 1991. On the mechanics of earthquake afterslip. J. Geophys. Res. 96 (B5), 8441–8452. https://doi.org/10.1029/91JB00275.

Meade, B.J., 2024. Kinematic afterslip patterns. Geophys. Res. Lett. 51 (1). https://doi.org/10.1029/2023GL105797.

Meyer, G.G., Brantut, N., Mitchell, T.M., Meredith, P.G., 2019. Fault reactivation and strain partitioning across the brittle-ductile transition. Geology. https://doi.org/10.1130/G46516.1.

Miyazaki, S., Segall, P., Fukuda, J., Kato, T., 2004. Space time distribution of afterslip following the 2003 Tokachi-oki earthquake: implications for variations in fault zone frictional properties. Geophys. Res. Lett. (6), 31. https://doi.org/10.1029/2003gl019410.

Ozawa, S., Nishimura, T., Munekane, H., Suito, H., Kobayashi, T., Tobita, M., Imakiire, T., 2012. Preceding, coseismic, and postseismic slips of the 2011 Tohoku earthquake, Japan. J. Geophys. Res.: Solid Earth 117 (B7). https://doi.org/10.1029/2011JB009120.

Passelègue, F.X., Almakari, M., Dublanchet, P., Barras, F., Fortin, J., Violay, M., 2020. Initial effective stress controls the nature of earthquakes. Nat. Commun. 11 (1), 1–8. https://doi.org/10.1038/s41467-020-18937-0.

Passelègue, F.X., Schubnel, A., Nielsen, S., Bhat, H.S., Deldicque, D., Madariaga, R., 2016. Dynamic rupture processes inferred from laboratory microearthquakes. J. Geophys. Res.: Solid Earth 121 (6), 4343–4365. https://doi.org/10.1002/2015JB012694.

Perfettini, H., Ampuero, J.P., 2008. Dynamics of a velocity strengthening fault region: implications for slow earthquakes and postseismic slip. J. Geophys. Res.: Solid Earth 113 (B9). https://doi.org/10.1029/2007JB005398.

Perfettini, H., Avouac, J.-P., 2004. Postseismic relaxation driven by brittle creep: a possible mechanism to reconcile geodetic measurements and the decay rate of aftershocks, application to the Chi-Chi earthquake, Taiwan. J. Geophys. Res.: Solid Earth 109 (B2). https://doi.org/10.1029/2003JB002488.

Perfettini, H., Avouac, J.P., 2007. Modeling aftership and aftershocks following the 1992 Landers earthquake. J. Geophys. Res.: Solid Earth 112 (B7). https://doi.org/10.1029/2006JB004399.

Perfettini, H., Avouac, J.P., Tavera, H., Kositsky, A., Nocquet, J.M., Bondoux, F., Chlieh, M., Sladen, A., Audin, L., Farber, D.L., Soler, P., 2010. Seismic and aseismic slip on the Central Peru megathrust. Nature 465 (3894), 78–81. https://doi.org/10.1038/nature09062.

Pozzi, G., Scuderi, M.M., Tinti, E., Nazzari, M., Collettini, C., 2022. The role of fault rock fabric in the dynamics of laboratory faults. J. Geophys. Res.: Solid Earth 127 (6). https://doi.org/10.1029/2021JB023779.

Rice, J.R., Gu, J.C., 1983. Earthquake aftereffects and triggered seismic phenomena. Pure Appl. Geophys. 121 (2), 187–219. https://doi.org/10.1007/BF02590135.

Ruina, A., 1983. Slip instability and state variable friction law. J. Geophys. Res. 88, 10359–10370. https://doi.org/10.1029/JB088iB12p10359.

Schmid, S.M., Paterson, M.S., Boland, J.N., 1980. High temperature flow and dynamic recrystallization in Carrara marble. Tectonophysics. 65 (3–4), 245–280. https://doi.org/10.1016/0040-1951(80)90077-3.

Scholz, C.H., 2019. The mechanics of earthquakes and faulting. The Mechanics of Earthquakes and Faulting, 3rd ed. Cambridge University Press. https://doi.org/10.1017/9781316681473.

Scuderi, M.M., Collettini, C., Viti, C., Tinti, E., Marone, C., 2017. Evolution of shear fabric in granular fault gouge from stable sliding to stick slip and implications for fault slip mode. Geology. 45 (8), 731–734. https://doi.org/10.1130/G39033.1.

Smith, S.W., Wyss, M., 1968. Displacement on the San Andreas fault subsequent to the 1966 Parkfield earthquake. Bull. Seismol. Soc. Am. 58 (6), 1955–1973. https://doi.org/10.1785/BSSA0580061955.

Song, J.Y., McLaskey, G.C., 2024. Laboratory earthquake ruptures contained by velocity strengthening fault patches. J. Geophys. Res.: Solid Earth 129 (4), 1–16. https://doi.org/10.1029/2023JB028509.

Thompson, B.D., Young, R.P., Lockner, D.A., 2009. Premonitory acoustic emissions and stick-slip in natural and smooth-faulted Westerly granite. J. Geophys. Res.: Solid Earth 114 (B2). https://doi.org/10.1029/2008JB005753.

Tullis, J., Yund, R.A., 1977. Experimental deformation of dry westerly granite. J. Geophys. Res. 82 (36), 5705–5718. https://doi.org/10.1029/JB082i036p05705.

Twardzik, C., Vergnolle, M., Sladen, A., Tsang, L.L.H., 2021. Very early identification of a bimodal frictional behavior during the post-seismic phase of the 2015 Mw 8.3 Illapel, Chile, earthquake. Solid Earth 12 (11), 2523–2537. https://doi.org/10.5194/se-12-2523-2021.

Verberne, B.A., Niemeijer, A.R., Bresser, J.H.P.De, Spiers, C.J, 2015. Mechanical behavior and microstructure of simulated calcite fault gouge sheared at 20–600°C: implications for natural faults in limestones. J. Geophys. Res.: Solid Earth 120 (12), 8169–8196. https://doi.org/10.1002/2015JB012292.

Verberne, B.A., Spiers, C.J., Niemeijer, A.R., De Bresser, J.H.P., De Winter, D.A.M., Plümper, O., 2014. Frictional properties and microstructure of calcite-rich fault gouges sheared at sub-seismic sliding velocities. Pure Appl. Geophys. 171 (10), 2617–2640. https://doi.org/10.1007/s00024-013-0760-0.

Wimpenny, S., Copley, A., Ingleby, T., 2017. Fault mechanics and post-seismic deformation at Bam, SE Iran. Geophys. J. Int. 209 (2), 1018–1035. https://doi.org/10.1093/gji/ggx065.

Wong, T.F., 1982. Micromechanics of faulting in westerly granite. Int. J. Rock Mech. Min. Sci. 19 (2), 49–64. https://doi.org/10.1016/0148-9062(82)91631-X.

Yagi, Y., Kikuchi, M., Nishimura, T., 2003. Co-seismic slip, post-seismic slip, and largest aftershock associated with the 1994 Sanriku-haruka-oki, Japan, earthquake. Geophys. Res. Lett. 30 (22). https://doi.org/10.1029/2003GL018189.

Yagi, Y., Kikuchi, M., Sagiya, T., 2001. Co-seismic slip, post-seismic slip, and aftershocks associated with two large earthquakes in 1996 in Hyuga-nada, Japan. Earth, Planets Space 53 (8), 793–803. https://doi.org/10.1186/BF03351677.